

Naive Gabor Networks

Chenying Liu, Jun Li
School of Geography and Planning
Sun Yat-sen University

{liuchy23@mail2, lijun48@mail}.sysu.edu.cn

Antonio J. Plaza
Hyperspectral Computing Laboratory
University of Extremadura
aplaza@unex.es

Lin He
School of Automation Science and Engineering
South China University of Technology

helin@scut.edu.cn

Shutao Li
College of Electrical and Information Engineering
Hunan University
shutao_li@hnu.edu.cn

Bo Li
School of Computer Science and Engineering
Beihang University
boli@buaa.edu.cn

Abstract

In this paper, we introduce naive Gabor Networks or Gabor-Nets which, for the first time in the literature, design and learn convolutional kernels strictly in the form of Gabor filters, aiming to reduce the number of parameters and constrain the solution space for convolutional neural networks (CNNs). In comparison with other Gabor-based methods, Gabor-Nets exploit the phase offset of the sinusoid harmonic to control the frequency characteristics of Gabor kernels, being able to adjust the convolutional kernels in accordance with the data from a frequency perspective. Furthermore, a fast 1-D decomposition of the Gabor kernel is implemented, bringing the original quadratic computational complexity of 2-D convolutions to a linear one. We evaluated our newly developed Gabor-Nets on two remotely sensed hyperspectral benchmarks, showing that our model architecture can significantly improve the convergence speed and the performance of CNNs, particularly when very limited training samples are available.

1. Introduction

CNNs have been widely employed for two important computer vision tasks, *i.e.*, feature extraction and classification. Different from traditional methods, which cope with the two aforementioned tasks individually (*e.g.*, using hand-crafted features and classifiers with predefined hyperparameters), CNNs –as a typical deep learning model– jointly

learn the two parts in a data-driven context. On the one hand, CNNs are capable to capture high-level features, and the learned feature representations are more robust and expressive than the hand-crafted ones, thus enhancing the subsequent classification. On the other hand, the parameters can be optimized in accordance with the data characteristics, leading to more effective models. However, deep learning methods suffer from a challenging demand for training samples in order to avoid overfitting, due to the huge number of parameters involved. Also, the black-box property of CNNs often leads to a lack of interpretability. Furthermore, finding optimal weights for CNNs is a non-convex problem, affected by many local minima and flat regions [2]. In fact, the gradient descend back-propagation is a local search algorithm, which easily converges to bad/spurious local minima when using a random initialization scheme [5].

To tackle these issues, a recent trend is to embed *a priori* knowledge into deep methods to refine model architectures. For example, Shamir [28] and Tian [31] showed that the adoption of Gaussian assumptions on the input distribution can assist the successful training of neural networks. Chen *et al.* [36, 37] overcame the contradiction between a small training size and a large parameter space through the integration of Bayesian modeling into neural networks. These previous works reveal that *a priori* knowledge exhibits good potential in increasing the reliability and improving the generalization of deep models. Concerning CNNs, as the random initialization and training of convolutional kernels are two major sources of instability in the architectures, *a priori* knowledge, such as harmonics, has been adopted to con-

strain convolutional kernels for achieving more robust models. For instance, circular harmonics are employed to equip CNNs with both translation and rotation equivariant kernels [32, 33]. The circular harmonics are steerable filters, which means that a filter of arbitrary orientation can be represented by a linear combination of a set of filter bases.

Apart from circular harmonics, Gabor harmonics are also widely used. Studies on the cat striate cortex show that the Gabor harmonic could provide a reasonably accurate modeling for the receptive fields of simple cells [9, 13, 23]. While CNNs are inspired by the structure of the mammalian visual system, it is plausible to constrain the convolutional kernels in shallow layers with the form of Gabor harmonics. Furthermore, as a powerful tool for feature extraction, Gabor filters are able to achieve optimal joint resolution in both space and frequency domains. Thus, it is very likely that they can work in deep layers present in CNNs using multi-layer Gabor features.

In this paper, we introduce *naive Gabor Networks*, or, Gabor-Nets, where *naive* refers to the fact that we straightforwardly replace standard convolutional kernels by Gabor filters. This is in fact the main difference between our proposed Gabor-Nets and standard CNNs, and also the main difference between the proposed Gabor-Nets and other Gabor-based CNNs. To the best of our knowledge, this is the first attempt in the literature to both design and learn the CNN convolutions strictly in the form of Gabor kernels. The main contributions of our newly developed Gabor-Nets can be summarized as follows:

- Gabor-Nets use Gabor filters as convolutional kernels to construct feed forward CNNs. Accordingly, in the back propagation stage, Gabor kernels are tuned in terms of Gabor parameters, *i.e.*, the ones used to generate Gabor kernels, leading to a reduction of parameters that benefits the training process of CNNs, requiring less training samples and converging faster.
- Gabor-Nets exploit the phase offsets of the sinusoid harmonics, which are generally disregarded by other Gabor-based methods, aimed at tuning the frequency response characteristics of filters. This leads to a more computationally efficient network structure.
- A final contribution is a fast decomposition implementation of the Gabor convolutions that brings the original quadratic computational complexity of 2-D convolutions to a linear one, significantly reducing the computational complexity for the networks implemented with our decomposed Gabor convolutions.

2. Related work

Here we first review some works focusing on traditional Gabor filters and then discuss CNNs with Gabor integrated.

2.1. Hand-crafted Gabor filters

From a signal processing perspective, Gabor harmonics maximize joint time/frequency or space/frequency resolutions [6], making them ideal for computer vision tasks. Hand-crafted Gabor filters have achieved great success in many applications, such as texture classification [10, 24], face and facial expression recognition [19, 27], palmprint recognition [35], edge detection [20], remote sensing image classification [7, 11], and so on [30]. Specifically, they utilize a bank of Gabor filters to extract features under selected orientations and scales. That is, hand-crafted Gabor features are just single-layer features with predefined parameters.

2.2. Gabor-based CNNs

Multiple approaches have tried to incorporate Gabor harmonics into CNNs, aiming at reducing parameters or equipping CNNs with orientation selectivity. Existing works can be categorized into two main groups, *i.e.*, those using Gabor feature representations and those using Gabor filters.

On the one hand, hand-crafted Gabor features were used to mitigate the negative effects introduced by the lack of training samples in CNNs. For example, Hosseini *et al.* [8] utilized the Gabor features combined with original images as inputs for CNN-based age and gender classification. Yao *et al.* [34] used Gabor features to pre-train CNNs before fine-tuning. In [4], Gabor features extracted on PCA features derived from hyperspectral images were fed into CNNs for classification purposes. Furthermore, Shi *et al.* [29] also achieved good performance by integrating CNN features and Gabor-based features for SVM-based ship classification, where Gabor based features could make up for the loss of rotation information in CNNs. Similar works can be found in [17, 25].

On the other hand, a recent trend is to manipulate certain layers or kernels of CNNs with Gabor filters, since many kernels in shallow layers of the CNN are similar to Gabor filters. Jiang *et al.* [12] replaced the first layer of a CNN with a bank of Gabor filters predefined with different orientations and shapes. The first layer Gabor filters can be fixed, as explained in [1], or tuned in the back propagation process, as indicated in [3] where, in fact, Gabor filters were used for initialization purposes. Moreover, to reduce the training complexity, Sarwar *et al.*, [26] replaced some kernels in the intermediate layers with fixed Gabor filters and achieved better results than original CNNs. More recently, Luan *et al.* [18] incorporated Gabor filters into the convolutional kernels as a modulation process. Gabor convolutional networks (GCNs), based on Gabor orientation filters which are generated using hand-crafted Gabor filters to modulate the learnable convolutional kernels, are capable to capture more robust output features to orientation and scale changes with less parameters. However, GCNs still manipulate hand-crafted Gabor filters to design the convolutional

kernels. That is, GCNs only use Gabor-like kernels.

3. Preliminaries

Let (x, y) denote the space domain of an image. A general 2-D Gabor filter in this context can be mathematically formulated by using a Gaussian envelope modulated sinusoid harmonic, as follows:

$$\mathbf{G}(x, y) = \frac{1}{2\pi\sigma_x\sigma_y} \exp\left\{-\frac{1}{2}\left(\frac{x_r^2}{\sigma_x^2} + \frac{y_r^2}{\sigma_y^2}\right)\right\} \times \exp\{j(x\omega_x + y\omega_y)\}, \quad (1)$$

where σ_x and σ_y are the scales along the two axes of the Gaussian envelope, $x_r = x \cos \phi + y \sin \phi$ and $y_r = -x \sin \phi + y \cos \phi$ are the rotated coordinates of x and y , with a given angle ϕ , $\omega_x = |\omega| \cos \theta$ and $\omega_y = |\omega| \sin \theta$ are the projections of a given angular frequency ω onto x and y -directions, respectively, θ is the angle between ω and the x -direction, $|\omega| = (\omega_x^2 + \omega_y^2)^{\frac{1}{2}}$ is the magnitude of ω (hereinafter replaced by ω) and j is the imaginary unit.

For designing biologically inspired Gabor filters, we set $\phi = \theta$ [13]. To simplify the gradient calculation of θ , we set $\sigma_x = \sigma_y = \sigma$, so that the Gaussian envelope is invariant to rotation. With Euler's relation, let $M = x\omega_x + y\omega_y$ hereinafter, we can rewrite the 2-D Gabor filter in the following complex form:

$$\mathbf{G}(x, y) = K \times \exp\{jM\} = K \cos M + jK \sin M, \quad (2)$$

where $K = \frac{1}{2\pi\sigma^2} \exp\{-\frac{x^2+y^2}{2\sigma^2}\}$ is the rotation-invariant Gaussian envelope. The Gabor filter in (2), which focuses on orientations and frequencies, is the general form used in most methods. However, there is an important term missing, namely, the phase offset of the sinusoid harmonic, P , which determines the symmetry of Gabor filters. Taking P into account, the general 2-D Gabor filter becomes

$$\mathbf{G}(x, y) = K \times \exp\{j(M + P)\}. \quad (3)$$

Accordingly, its complex form is as follows,

$$\mathbf{G}(x, y) = \Re\{\mathbf{G}(x, y)\} + j\Im\{\mathbf{G}(x, y)\} = K \cos(M + P) + jK \sin(M + P). \quad (4)$$

Specifically, for the real part $\Re\{\mathbf{G}(x, y)\}$, if $P = 0$ or π , it is symmetric with respect to the filter center; if $P = (\pi/2)$ or $(3\pi/2)$, it is antisymmetric, and all other cases are asymmetric. It is believed that a cell with a symmetric receptive field will react strongly to the bars coinciding in direction, width and polarity, with the central lobe of the receptive field [22]. Based on this observation, it generally uses the real part of (2) with $P = 0$ to construct

orientation-selective and frequency-specific filters for feature extraction. Quite opposite, in the following we argue that the phase offset P has a close relationship with the frequency characteristics of Gabor filters, playing a dominant role in Gabor-Nets.

4. Proposed method

In this section, we present Gabor-Nets in detail. Before introducing Gabor-Nets, we first present the 2-D Gabor kernel, followed by a 1-D fast decomposition implementation.

4.1. Gabor kernel

Considering the imagery part of the 2-D Gabor filter with a phase offset P , we have,

$$\begin{aligned} \Im\{\mathbf{G}_P(x, y)\} &= K \sin(M + P) \\ &= K \cos\left(\frac{\pi}{2} - (M + P)\right) \\ &= K \cos\left(M + (P - \frac{\pi}{2})\right), \end{aligned} \quad (5)$$

that is,

$$\Im\{\mathbf{G}_P(x, y)\} = \Re\{\mathbf{G}_{(P-\frac{\pi}{2})}(x, y)\}. \quad (6)$$

As shown in (6), the imagery part with P is the same as the real counterpart yet with a phase offset of $(P - \pi/2)$. The one-to-one correspondence between the real and imaginary parts is illustrated in Figure 1.

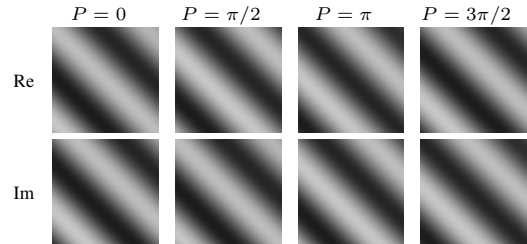


Figure 1. Real and imaginary parts of complex Gabor filters for a simple example with $\theta = \pi/4$, $\omega = \pi/100$, $\sigma = 30$, and different phase offsets. Note that the imagery part with a certain phase offset P is just the corresponding real one with $(P - \pi/2)$.

Therefore, in Gabor-Nets, we only employ the real parts for the construction of Gabor kernels, namely,

$$\mathbf{G}(x, y) = K \cos(M + P). \quad (7)$$

Obviously, without complex-valued operators, the Gabor kernels in (7) are featured with higher computational efficiency, yet little information loss, than those of (4).

4.2. Gabor kernel decomposition

Through a detailed inspection of (7), we can find out that the cosine harmonic used by the 2-D Gabor kernel is formed

by the coupling of x , y , and P . If we separate the Gaussian envelope K along the x and y -directions, (7) turns to (details in Supplementary Material):

$$\begin{aligned} \mathbf{G}(x, y) = & \cos P \cdot g_c^{(x)} \cdot g_s^{(y)} - \cos P \cdot g_s^{(x)} \cdot g_c^{(y)} \\ & - \sin P \cdot g_s^{(x)} \cdot g_c^{(y)} - \sin P \cdot g_c^{(x)} \cdot g_s^{(y)}, \end{aligned} \quad (8)$$

where

$$\begin{aligned} g_c^{(a)} &= \frac{1}{\sqrt{2\pi}\sigma} \exp\left(-\frac{a^2}{2\sigma^2}\right) \cos(a\omega_a), \\ g_s^{(a)} &= \frac{1}{\sqrt{2\pi}\sigma} \exp\left(-\frac{a^2}{2\sigma^2}\right) \sin(a\omega_a), \end{aligned}$$

with $a = x$ or y . As indicated in (8), a 2-D Gabor kernel is virtually formed by the weighted superposition of four sub-filters, each of which is constituted by the separable tensor product of two 1-D filters along the x - and y -directions, respectively. That means, under the decomposition form in (8), the original quadratic computational complexity of 2-D convolutions using (7) can be reduced to a linear one, in which case, with k being the kernel size, the complexity, associated with the kernels, is changed from $O(k^2)$ to $O(k)$.

Furthermore, it has been proven in [7] that, $g_c^{(a)}$ and $g_s^{(a)}$ are low-frequency pass and low-frequency resistant filters, respectively. Therefore, we can conclude that the four sub-filters are different in terms of frequency characteristics, whereas the phase offset term P dominates the proportion of them in a 2-D Gabor kernel via $\cos P$ and $\sin P$.

4.3. Gabor-Nets

In Gabor-Nets, the convolutional kernels are designed in the form of (8) in each layer, where the learned parameters are those used for Gabor kernel construction, $\{\theta, \omega, \sigma, P\}$, *i.e.*, the phase offset P , the scale σ , the magnitude of the angular frequency ω , and the angle between the angular frequency and the x -direction θ . For simplicity, we utilize \mathbf{G} in place of $\mathbf{G}(x, y)$, and $\{\theta_0, \omega_0, \sigma_0, P_0\}$ to represent the initialization of Gabor parameters hereinafter. As illustrated in Figure 2, unlike standard CNNs, in Gabor-Nets the number of output features in the l th convolutional layer is determined as $N_o = N_t \times N_m$, where N_t and N_m are the predefined number of θ s and ω s, respectively. Then, with N_i input features, the kernels in the l th layer are defined as

$$\mathbf{G}^{(l)} = \{\mathbf{G}_1^{(l)}, \mathbf{G}_2^{(l)}, \dots, \mathbf{G}_{N_o}^{(l)}\}, \quad (9)$$

where $\mathbf{G}_o^{(l)} = \{\mathbf{G}_{o,1}^{(l)}, \dots, \mathbf{G}_{o,N_i}^{(l)}\}$, $o = 1, 2, \dots, N_o$ is a set of N_i Gabor kernels corresponding to the N_i input features, which are used to generate the o th output feature. Notice that, within a set, the N_i kernels are initialized with the same θ_0 and ω_0 , and then are fine-tuned separately in a

data-driven context during the training. As a result, we can obtain the output features as follows,

$$\mathbf{O}^{(l)} = \{\mathbf{O}_1^{(l)}, \mathbf{O}_2^{(l)}, \dots, \mathbf{O}_{N_o}^{(l)}\}, \quad (10)$$

where $\mathbf{O}_o^{(l)} = \sum_i^{N_i} \mathbf{I}_i^{(l)} * \mathbf{G}_{o,i}^{(l)}$, for $o = 1, 2, \dots, N_o$, and $\mathbf{I}^{(l)} = \{\mathbf{I}_1^{(l)}, \dots, \mathbf{I}_{N_i}^{(l)}\}$ are the input features of the l th layer. For the first layer, $\mathbf{I}^{(l)}$ are the initial input features of the network, otherwise $\mathbf{I}^{(l)} = \mathbf{O}^{(l-1)}$.

Notice that the key difference between the proposed Gabor-Nets and standard CNNs is the design of convolutional kernels. Therefore, it is very easy to incorporate other CNN elements or tricks into Gabor-Nets, such as pooling, batch normalization, activation functions, etc.

Initialization of Gabor kernels In order to guarantee the effectiveness of Gabor kernels, we provide a general reliable initialization. Following the empirical settings for hand-crafted Gabor feature extraction, in order to cover as many orientations as possible, the θ_0 s are predefined as an evenly spaced sequence of $[0, \pi)$ based on N_t . Furthermore, the ω_0 s are set as a geometric sequence with an initial value of $(\pi/2)$ and a geometric progression of $(1/2)$ as in [7]. For example, as shown in Figure 2, to construct a Gabor convolutional layer using $N_t = 4$ and $N_m = 2$, we set θ_0 s to be 0, $(\pi/4)$, $(\pi/2)$, $(3\pi/4)$, and ω_0 s to be $(\pi/2)$, $(\pi/4)$, respectively. While, the σ_0 s are set to be one quarter of the kernel size. With respect to the phase offset P , we randomly initialize P_0 s within $[0, 2\pi)$, *i.e.*, both $\sin P_0$ and $\cos P_0$ within $[-1, 1]$ in each layer. As discussed before, P dominates the frequency characteristics of Gabor kernels via $\cos P$ and $\sin P$. Therefore, such initialization scheme for P can increase the diversity of Gabor kernels, thus promoting the robustness of Gabor-Nets.

Updating of Gabor kernels In the back propagation of Gabor-Nets, we update the convolutional kernels as a whole by adjusting the aforementioned Gabor parameters, rather than directly updating each element. Therefore, the gradients of the Gabor parameters are aggregated from all the elements in the kernels as follows:

$$\begin{aligned} \delta_\tau &= \frac{\partial L}{\partial \tau} = \sum_{x,y} \delta_{\mathbf{G}} \circ \frac{\partial \mathbf{G}}{\partial \tau}, \\ \tau &\leftarrow \tau - \delta_\tau, \quad \text{for } \tau = \{\theta, \omega, \sigma, P\}, \end{aligned} \quad (11)$$

where $\delta_{\mathbf{G}}$ is the gradient of the training loss L w.r.t. \mathbf{G} , \circ is the Hadamard product, and

$$\frac{\partial \mathbf{G}}{\partial P} = -K \sin(x\omega_x + y\omega_y + P), \quad (12)$$

$$\frac{\partial \mathbf{G}}{\partial \theta} = \frac{\partial \mathbf{G}}{\partial P} \circ (-x\omega_y + y\omega_x), \quad (13)$$

$$\frac{\partial \mathbf{G}}{\partial \omega} = \frac{\partial \mathbf{G}}{\partial P} \circ (x \cos \theta + y \sin \theta), \quad (14)$$

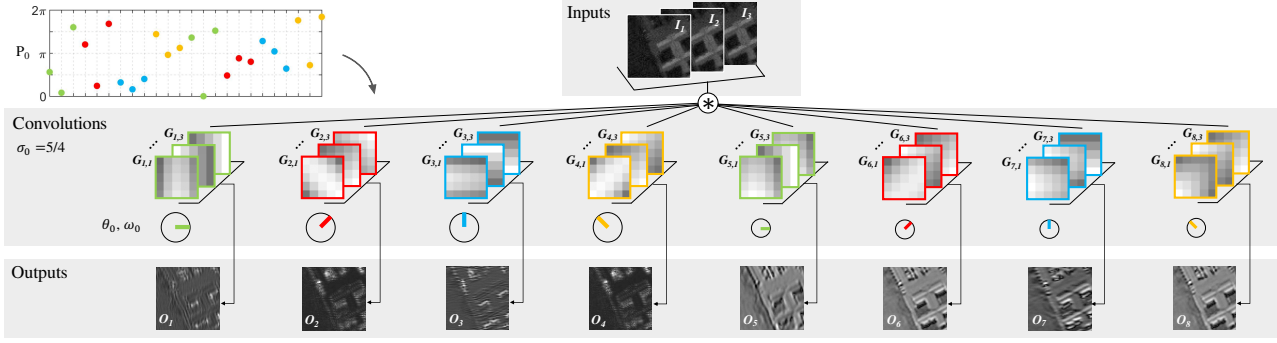


Figure 2. Forward process of one convolutional layer in Gabor-Nets, with the number of input features $N_i = 3$ and the kernel size $k = 5$. The kernels are constructed using four θ_0 s and two ω_0 s, *i.e.*, $N_t = 4$ and $N_m = 2$, where the ones marked by the same color and the same size of circles are initialized with the same θ_0 and ω_0 , respectively. Therefore, there are 8 output features in total, *i.e.*, $N_0 = 4 \times 2 = 8$. Furthermore, σ s are all initialized with $k/4 = 5/4$, and P s are randomly initialized within the range $[0, 2\pi)$.

$$\frac{\partial \mathbf{G}}{\partial \sigma} = \mathbf{G} \circ \left(\frac{x^2 + y^2}{\sigma^3} - \frac{2}{\sigma} \right). \quad (15)$$

4.4. Adaptive frequency response property

Based on the kernel decomposition strategy introduced in Section 4.2, taking the real part of (2) into account, *i.e.*, the real part of a general 2-D Gabor filter without P , we have,

$$\mathbf{G}' = g_c^{(x)} \cdot g_c^{(y)} - g_s^{(x)} \cdot g_s^{(y)}. \quad (16)$$

For simplicity, here we use \mathbf{G}' to denote the real part of the Gabor filter without P . As observed in (16), the real part of the Gabor filter without P , which is widely used in hand-crafted Gabor feature extraction, is composed of two 2-D sub-filters, each of which is associated with two 1-D filters. Recall that, $g_c^{(a)}$ is low-frequency pass, while $g_s^{(a)}$ is low-frequency resistant. Therefore, it can be inferred that the two 2-D sub-filters are low-frequency pass and low-frequency resistant, respectively. If such Gabor filters are integrated into CNNs, the fundamental properties of kernels, *i.e.*, the frequency response characteristics, would be changed slightly during the parameter tuning.

Then, we rewrite the decomposition form of (7) using the trigonometric formula as follows¹,

$$\mathbf{G} = g_{c,p}^{(x)} \cdot g_c^{(y)} - g_{s,p}^{(x)} \cdot g_s^{(y)}, \quad (17)$$

where

$$g_{c,p}^{(x)} = \frac{1}{\sqrt{2\pi}\sigma} \exp\left(-\frac{x^2}{2\sigma^2}\right) \cos(x\omega_x + P), \quad (18)$$

and

$$g_{s,p}^{(x)} = \frac{1}{\sqrt{2\pi}\sigma} \exp\left(-\frac{x^2}{2\sigma^2}\right) \sin(x\omega_x + P). \quad (19)$$

¹It is identical to allocate the phase offset P with x or y .

Comparing (17) with (16), we can find out that, with P added, the 1-D Gaussian-modulated cosine or sine harmonics along the x -direction become $g_{c,p}^{(x)}$ and $g_{s,p}^{(x)}$, respectively. For a more detailed investigation on the properties of Gabor kernels with varying P s, given ω_0 of ω_x , their mathematical representations in the frequency domain are calculated as follows (details in Supplementary Material),

$$\hat{g}_{c,p}(\omega) = \frac{1}{2}(A + B) \cos P + \frac{1}{2}j(A - B) \sin P, \quad (20)$$

and

$$\hat{g}_{s,p}(\omega) = \frac{1}{2}(A + B) \sin P - \frac{1}{2}j(A - B) \cos P, \quad (21)$$

where $A = \exp\left(-\frac{\sigma^2(\omega - \omega_0)^2}{2}\right)$, and $B = \exp\left(-\frac{\sigma^2(\omega + \omega_0)^2}{2}\right)$.

Then we can obtain the corresponding squared magnitudes of frequency as follows,

$$|\hat{g}_{c,p}(\omega)|^2 = \frac{1}{4} \exp(-\sigma^2(\omega - \omega_0)^2) + \frac{1}{4} \exp(-\sigma^2(\omega + \omega_0)^2) + \frac{1}{2} \cos(2P) \exp(-\sigma^2(\omega^2 + \omega_0^2)), \quad (22)$$

and

$$|\hat{g}_{s,p}(\omega)|^2 = \frac{1}{4} \exp(-\sigma^2(\omega - \omega_0)^2) + \frac{1}{4} \exp(-\sigma^2(\omega + \omega_0)^2) - \frac{1}{2} \cos(2P) \exp(-\sigma^2(\omega^2 + \omega_0^2)). \quad (23)$$

Set ω in (22) and (23) to be zero, we have

$$|\hat{g}_{c,p}(0)|^2 = \frac{1}{2}[1 + \cos(2P)] \exp(-\sigma^2\omega_0^2), \quad (24)$$

and,

$$|\hat{g}_{s,p}(0)|^2 = \frac{1}{2}[1 - \cos(2P)] \exp(-\sigma^2\omega_0^2). \quad (25)$$

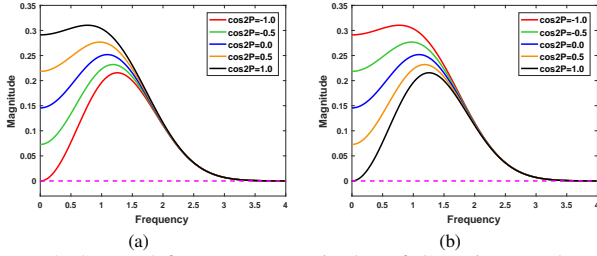


Figure 3. Squared frequency magnitudes of Gaussian enveloped (a) cosine and (b) sinusoidal harmonics with varying values of P .

As shown in (24) and (25), when $\cos(2P)$ is approaching -1 , $|\hat{g}_{c,p}(0)|^2$ and $|\hat{g}_{s,p}(0)|^2$ are decreasing to and increasing away from 0, respectively (which implies that the low-frequency resistance of $g_{c,p}^{(x)}$ is being enforced, while $g_{s,p}^{(x)}$ behaves more like a low-pass filter). The situation is opposite when $\cos(2P)$ is approaching 1. Figure 3 shows the appearance of the squared magnitudes in the frequency domain with varying values of P . Clearly, the frequency response characteristics of $g_{c,p}^{(x)}$ and $g_{s,p}^{(x)}$ significantly change when P varies. Notice that $g_{c,p}^{(x)}$ and $g_{s,p}^{(x)}$ are special cases for $g_{c,p}^{(x)}$ and $g_{s,p}^{(x)}$ at $\cos(2P) = 1$. Therefore, taking P into consideration, Gabor-Nets can effectively adapt the frequency properties of Gabor kernels in a data-driven context.

5. Experiments

In this section, we first evaluate the proposed Gabor-Nets on two remotely sensed hyperspectral datasets for pixel-wise classification purposes. After that, we investigate some of the properties of Gabor-Nets.

5.1. Classification results

Classification is one of the most important tasks in hyperspectral image processing. To conduct pixel-wise classification using CNNs, a general implementation scheme is to utilize squared patches centered on the given samples as the input features for CNNs.

Pavia University Scene This scene² is a benchmark hyperspectral dataset for classification, which was collected by the Reflective Optics Imaging Spectrometer System (ROSIS) sensor over the urban area of the University of Pavia, Italy, in 2003. The image contains 610×340 samples with a spatial resolution of 1.3m, and 103 spectral bands ranging from 0.43 to 0.86 μm . The ground truth contains 42776 labeled samples within 9 classes of interest including Asphalt (6631), Meadows (18649), Gravel (2099), Trees (3064), Painted metal sheets (1345), Bare soil (5029), Bitumen (1330), Self-blocking bricks (3682), and Shadows

²Both datasets can be downloaded from <https://www.sipeo.bgu.tum.de/downloads>.

(947). For the input patches, we set the size to be 15, and used the images of each band as initial input features.

We used two convolutional blocks and a fully connected block to construct the network architecture of Gabor-Nets (details in Supplementary Material). Each convolutional block contains two Gabor convolutional layers with a kernel size of 5, a ReLU nonlinearity layer, and a Batch Normalization layer. We set N_t , N_m as 4, 4 for the first block, and 8, 4 for the second one, respectively. The fully connected block contains two layers, the last one of which is used for classification. We used the cross-entropy loss as the objective function and Adam as the optimizer. For comparison, we also implemented the corresponding versions of standard CNNs, *i.e.*, those with the same architecture as Gabor-Nets yet using standard convolutional kernels, and the traditional supervised methods on the hand-crafted Gabor features using a multinomial logistic regression (MLR) classifier and a support vector machine (SVM) classifier, respectively. Table 1 lists the results obtained after averaging 5 Monte Carlo runs, and some others by existing state-of-the-art CNN based hyperspectral classification methods. It can be seen that our Gabor-Nets obtained very competitive results when compared to the others. The improvements are quite significant, especially when the training samples are limited. This is expected since Gabor kernels are parameter-economic. As shown in Table 2, the number of parameters in Gabor-Nets is much smaller than that in standard CNNs.

Method	Test Accuracy (%)	
	100/class	200/class
Gabor-MLR	93.83 \pm 0.63	95.44 \pm 0.25
Gabor-SVM	92.15 \pm 0.28	93.90 \pm 0.37
3-D CNN [21]*	94.37	98.06
CDCNN [14]*	-	95.97
Gabor as inputs[4]*	-	97.33
CNN-PPF[15]*	-	97.63
S-CNN[16]*	-	97.93
CNNs	92.73 \pm 1.74	97.27 \pm 0.47
Gabor-Nets	95.51 \pm 0.48	97.99 \pm 0.19
CNNs+Aug.	95.55 \pm 1.03	97.95 \pm 0.75
Gabor-Nets+Aug.	97.68\pm0.74	98.88\pm0.35

Table 1. Test accuracies on the ROSIS Pavia University scene obtained with 100 and 200 training samples per class, respectively, where Aug. represents the implementation with data augmentation, and * represents Others' implementation.

Figure 4 plots the training accuracies and losses of the first 50 epochs from CNNs and Gabor-Nets. It can be seen that Gabor-Nets initially exhibit higher training accuracies and smaller losses, and then converge faster than the standard ones, which verifies the effectiveness of Gabor kernels.

Indian Pines Scene The second scene is the well-known

Method	#params		
	/kernel	Pavia	Indian
CNNs	25	86k	125k
Gabor-Nets	4	14k	20k

Table 2. Number of parameters, where the convolutional kernel size is set to 5 in both cases.

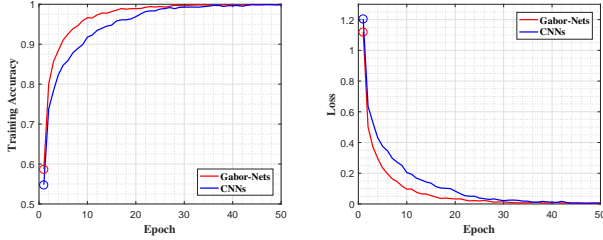


Figure 4. Training accuracies (a) and losses (b) as functions of the number of epochs from Gabor-Nets and standard CNNs. The initial values are marked with circles.

Indian Pines dataset collected by the Airborne Visible Infrared Imaging Spectrometer (AVIRIS) sensor in 1992. This scene is composed of 220 spectral bands with wavelength varying from 0.4 to 2.5 μm , and 145×145 pixels with a spatial coverage of $20\text{m} \times 20\text{m}$. In our experiments, we removed 20 bands due to noises and water absorption and the classes containing less than 200 samples in the ground-truth, resulting in 200 bands and 9345 labeled samples within 9 classes (see Figure 5). This scene is challenging for CNN based classification due to the small data size. Thus, the purpose here is to evaluate the capability of Gabor-Nets to cope with the cases of limited training samples.

For this scene, we utilized a similar network architecture to the previous one, except for the number of initial input features as 200. Tables 2 and 3 list the number of parameters, and the test accuracies obtained with different numbers of training samples, respectively. Obviously, Gabor-Nets, with less parameters, outperform others in all the cases, specially when the training samples are very limited. The excellent performance of Gabor-Nets can also be observed in Figure 5, where the classification map obtained by Gabor-Nets is smoother than the one provided by CNNs.

Method	Test Accuracy (%)		
	40/class	60/class	80/class
Gabor-MLR	85.45 \pm 0.92	88.78 \pm 1.17	89.98 \pm 0.94
Gabor-SVM	80.41 \pm 0.93	84.92 \pm 1.16	87.30 \pm 0.52
CNNs	90.11 \pm 1.16	93.51 \pm 1.30	96.50 \pm 0.77
Gabor-Nets	91.49\pm0.86	94.18\pm1.09	96.69\pm0.44

Table 3. Test accuracies on the AVIRIS Indian Pines scene obtained with 40, 60, and 80 training samples per class, respectively.

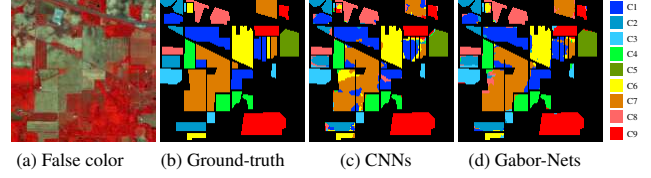


Figure 5. The obtained classification maps with 40 training samples per class for the AVIRIS Indian Pines scene. The C1-C9 classes are Alfalfa (1434), Corn-no till (834), Corn-min till (497), Grass/Trees (747), Hay-windrowed (489), Soybeans-no till (968), Soybeansmin till (2468), Wheat (614), and Woods (1294), where the numbers of samples within each class are listed in brackets.

5.2. Model Insight

To analyze the mechanism behind Gabor-Nets, we investigate some of the properties of Gabor-Nets in terms of Gabor parameters. Specifically, the following takes for example the Gabor-Nets trained on the Pavia University scene using 100 training samples per class.

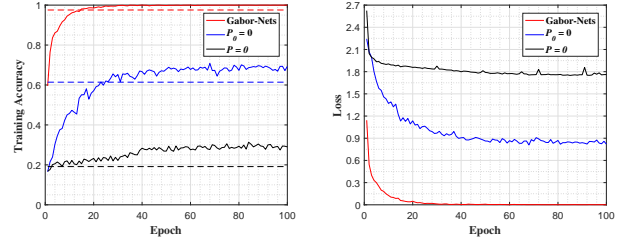


Figure 6. Training accuracies (a) and losses (b) as functions of the number of epochs, where three cases of Gabor-Nets are shown: the one that we proposed (red), the one with P_s initialized as 0, i.e., $P_0 = 0$ (blue), and the one without P , i.e., $P = 0$ (black). The dashed lines indicate their test accuracies after 100 epochs.

Phase offsets As stated above, in Gabor-Nets, the phase offset P is an important parameter which controls the frequency characteristics of Gabor kernels. To verify the effectiveness of P , we implemented two variants of Gabor-Nets, i.e., the one with all P_s initialized as 0, that is $P_0 = 0$; and the one without P , that is $P = 0$. Figure 6 shows the training accuracies and losses as functions of the number of epochs. Impressively, by constructing Gabor kernels with P_s randomly initialized in $[0, 2\pi)$, the performance of Gabor-Nets is significantly boosted when compared to the other two cases, where Gabor-Nets show around 35% and 75% improvements on them, respectively. Quite opposite, without P a slight improvement can be obtained during the training, although the other parameters, like θ , ω , and σ can be adjusted in a data-driven context. We argue that this is because the Gabor kernels are restricted to only two 2-D components, i.e., the low-pass one and the band-pass one, thus leading to a severe loss of information. Furthermore, the performance of the case with $P_0 = 0$ is limited, despite outperforming the one without P . Recall that the gradi-

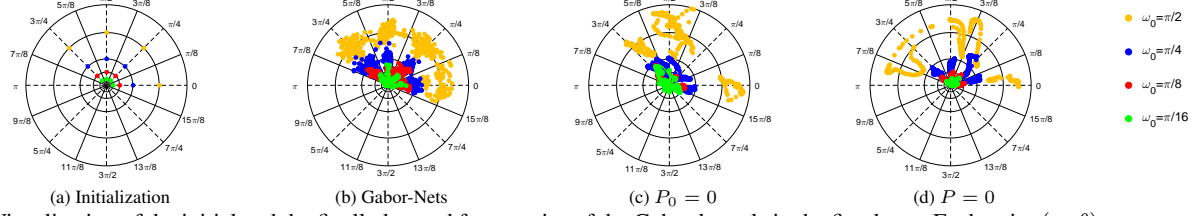


Figure 7. Visualization of the initial and the finally learned frequencies of the Gabor kernels in the first layer. Each point (ω, θ) corresponds to a learned kernel constructed with the angle θ and the frequency magnitude ω . The colored points represent the kernels with different ω_0 s. The circles (from inside out) represent the cases where ω is $\pi/16$, $\pi/8$, $\pi/4$, $\pi/2$, and 2.4, respectively. Notice that all the learned frequencies in the cases (b)-(d) used the same initialization shown in (a). (Best viewed in color.)

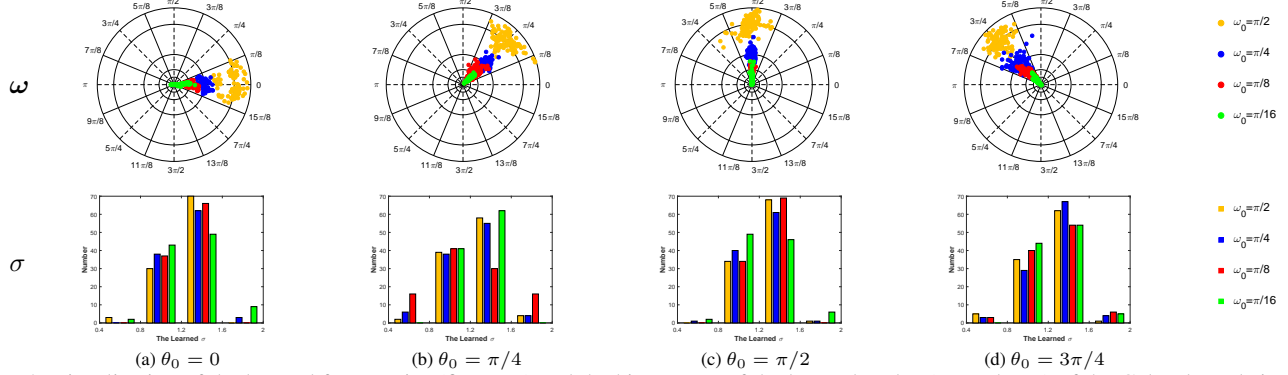


Figure 8. Visualization of the learned frequencies (first row) and the histograms of the learned scales (second row) of the Gabor kernels in the first layer, where each column and each color show the learned parameters initialized with the same θ_0 s and ω_0 s, respectively, and all the σ s are initialized as $(\text{kernel size})/4$, i.e., $(5/4)$ in our experiments. That is, the points and the bars marked with the same color in a column correspond to one of the 16 output features in the first layer. The circles from inside out represent the cases where ω is $(\pi/16)$, $(\pi/8)$, $(\pi/4)$, $(\pi/2)$, and 2, respectively. (Best viewed in color.)

ent descend back-propagation is a local search algorithm, in which a fixed initialization of P s would lead to a fixed local minimum. It can be anticipated that, for Gabor-Nets, more components are required to generate more discriminative features, since an initialization considering only two components leads to a bad local minimum.

Another interesting experiment explores the learned angular frequencies in each case. Figure 7 shows the final learned frequencies of Gabor kernels in the first layer in terms of their angles and magnitudes³. Noticeably, the learned frequencies of Gabor-Nets almost cover the whole semicircle region, while those in the other cases are only distributed at some local narrow regions, especially in the case without P , which reveals that Gabor-Nets have potential in the task of extracting features with any orientation and varying frequencies, instead of only some of their combinations. It can be inferred that the variety of P s in Gabor-Nets can benefit the learning of angular frequencies to some degree.

Parameters in traditional Gabor filters Here we analyze other parameters used in hand-crafted Gabor filter construction, i.e., the frequency angle θ , the frequency magnitude

ω , and the scale σ in Gabor-Nets. Figure 8 demonstrates the learned angular frequencies determined by θ s and ω s, and the histograms of the learned σ s of the Gabor kernels in the first layer, where each color in each column corresponds to a kernel bank used to generate an output feature, i.e., $G_o^{(1)}$. As shown in the first row, almost all the points gather in a θ_0 -centric sector region with an angle range of $(\pi/4)$, where those marked with different colors are well distributed around the arc corresponding to their ω_0 s. Namely, although the points in Figure 7 (b) almost cover the whole semicircle region, the points representing different kernel banks little overlap with each other. This means that, around θ_0 and ω_0 , the Gabor kernel banks can extract the features with varying θ s and ω s, rather than those intended for a single predetermined frequency as the hand-crafted Gabor filters do, thus making Gabor filters more powerful in Gabor-Nets. Furthermore, as shown in the second row, σ s are also adjusted during the training.

6. Conclusions and future lines

We presented *naive Gabor Networks*, i.e., Gabor-Nets, which, for the first time, design and learn convolutional kernels strictly in the form of Gabor filters, with much less pa-

³Those in the other layers can be seen in Supplementary Material.

rameters in comparison with traditional CNNs. By exploiting the phase offsets of sinusoid harmonics, Gabor-Nets are capable to tune the convolutional kernels for data-driven frequency responses. Furthermore, we propose a fast 1-D decomposition implementation of the Gabor convolutional kernel, leading to high efficiency in terms of computational complexity. Another important aspect is that, since we have only manipulated the way of kernel generation, Gabor-Nets can be easily implemented with other CNN tricks or structures. Our experiments on two real hyperspectral datasets show that Gabor kernels can significantly improve the convergence speed and the performance of CNNs, particularly in cases of very limited training samples. In the future, we will use Gabor-Nets for object detection and processing of natural images.

References

- [1] S. R. Andres Calderon and J. Victorino. Handwritten digit recognition using convolutional neural networks and gabor filters. In *the International Congress on Computational Intelligence (CIIC)*, 2003. 2
- [2] A. L. Blum and R. L. Rivest. Training a 3-node neural network is np-complete. *Neural Networks*, 5(1):9–28, Jan. 1992. 1
- [3] S.-Y. Chang and N. Morgan. Robust cnn-based speech recognition with gabor filter kernels. In *INTERSPEECH*, pages 905–909, 2014. 2
- [4] Y. Chen, L. Zhu, P. Ghamisi, X. Jia, G. Li, and L. Tang. Hyperspectral images classification with gabor filtering and convolutional neural network. *IEEE Geoscience and Remote Sensing Letters*, 14(12):2355–2359, Dec 2017. 2, 6
- [5] S. S. Du, J. D. Lee, Y. Tian, B. Poczos, and A. Singh. Gradient descent learns one-hidden-layer cnn: Don’t be afraid of spurious local minima. In *Proceedings of the Thirty-fifth International Conference on Machine Learning (ICML)*, 2018. 1
- [6] D. Gabor. Theory of communication. *Journal of the Institution of Electrical Engineers*, 93(26):429–257, January 1946. 2
- [7] L. He, J. Li, A. Plaza, and Y. Li. Discriminative low-rank gabor filtering for spectral-spatial hyperspectral image classification. *IEEE Transactions on Geoscience and Remote Sensing*, 55(3):1381–1395, March 2017. 2, 4
- [8] S. Hosseini, S. H. Lee, H. J. Kwon, H. I. Koo, and N. I. Cho. Age and gender classification using wide convolutional neural network and gabor filter. In *2018 International Workshop on Advanced Image Technology (IWAIT)*, pages 1–3, Jan 2018. 2
- [9] D. Hubel and T. Wiesel. Receptive fields and functional architecture in two nonstriate visual areas 18 and 19 of the cat. *Journal of neurophysiology*, 28:229289, March 1965. 2
- [10] M. Idrissa and M. Acheroy. Texture classification using gabor filters. *Pattern Recognition Letters*, 23(9):1095 – 1102, 2002. 2
- [11] S. Jia, L. Shen, J. Zhu, and Q. Li. A 3-d gabor phase-based coding and matching framework for hyperspectral imagery classification. *IEEE Transactions on Cybernetics*, 48(4):1176–1188, April 2018. 2
- [12] C. Jiang and J. Su. Gabor binary layer in convolutional neural networks. In *2018 25th IEEE International Conference on Image Processing (ICIP)*, pages 3408–3412, Oct 2018. 2
- [13] J. Jones and L. Palmer. An evaluation of the two-dimensional gabor filter model of simple receptive fields in cat striate cortex. *Journal of neurophysiology*, 58(6):12331258, December 1987. 2, 3
- [14] H. Lee and H. Kwon. Going deeper with contextual cnn for hyperspectral image classification. *IEEE Transactions on Image Processing*, 26(10):4843–4855, Oct 2017. 6
- [15] W. Li, G. Wu, F. Zhang, and Q. Du. Hyperspectral image classification using deep pixel-pair features. *IEEE Transactions on Geoscience and Remote Sensing*, 55(2):844–853, Feb 2017. 6
- [16] B. Liu, X. Yu, P. Zhang, A. Yu, Q. Fu, and X. Wei. Supervised deep feature extraction for hyperspectral image classification. *IEEE Transactions on Geoscience and Remote Sensing*, 56(4):1909–1921, April 2018. 6
- [17] T. Lu, M. Wu, and T. Lu. Face recognition via gabor and convolutional neural network. In *Ninth International Conference on Graphic and Image Processing (ICGIP 2017)*, 2017. 2
- [18] S. Luan, C. Chen, B. Zhang, J. Han, and J. Liu. Gabor convolutional networks. *IEEE Transactions on Image Processing*, 27(9):4357–4366, Sept 2018. 2
- [19] M. Lyons, S. Akamatsu, M. Kamachi, and J. Gyoba. Coding facial expressions with gabor wavelets. In *Proceedings of the Third IEEE International Conference on Automatic Face and Gesture Recognition (AFGR)*, pages 200–205, April 1998. 2
- [20] K. R. Namuduri, R. Mehrotra, and N. Ranganathan. Edge detection models based on gabor filters. In *Proceedings of the 11th International Conference on Pattern Recognition (ICPR)*, pages 729–732, Aug 1992. 2
- [21] M. Paoletti, J. Haut, J. Plaza, and A. Plaza. A new deep convolutional neural network for fast hyperspectral image classification. *ISPRS Journal of Photogrammetry and Remote Sensing*, 145:120 – 147, 2018. Deep Learning RS Data. 6
- [22] N. Petkov and P. Kruizinga. Computational models of visual neurons specialised in the detection of periodic and aperiodic oriented visual stimuli: bar and grating cells. *Biological Cybernetics*, 76(2):83–96, 1997. 3
- [23] D. A. Pollen and S. F. Ronner. Visual cortical neurons as localized spatial frequency filters. *IEEE Transactions on Systems, Man, and Cybernetics*, SMC-13(5):907–916, Sept 1983. 2
- [24] R. Porter and N. Canagarajah. Robust rotation-invariant texture classification: wavelet, gabor filter and gmrf based schemes. *IEE Proceedings - Vision, Image and Signal Processing*, 144(3):180–188, June 1997. 2
- [25] S. T. H. Rizvi, G. Cabodi, P. Gusmao, and G. Francini. Gabor filter based image representation for object classification. In *Proceedings of 2016 International Conference on Control, Decision and Information Technologies (CoDIT)*, pages 628–632, April 2016. 2

- [26] S. S. Sarwar, P. Panda, and K. Roy. Gabor filter assisted energy efficient fast learning convolutional neural networks. In *2017 IEEE/ACM International Symposium on Low Power Electronics and Design (ISLPED)*, pages 1–6, July 2017. 2
- [27] Y. C. See, N. M. Noor, J. L. Low, and E. Liew. Investigation of face recognition using gabor filter with random forest as learning framework. In *2017 IEEE Region 10 Conference (TENCON)*, pages 1153–1158, Nov 2017. 2
- [28] O. Shamir. Distribution-specific hardness of learning neural networks. *CoRR*, abs/1609.01037, 2016. 1
- [29] Q. Shi, W. Li, F. Zhang, W. Hu, X. Sun, and L. Gao. Deep cnn with multi-scale rotation invariance features for ship classification. *IEEE Access*, 6:38656–38668, 2018. 2
- [30] Z. Sun, G. Bebis, and R. Miller. On-road vehicle detection using evolutionary gabor filter optimization. *IEEE Transactions on Intelligent Transportation Systems*, 6(2):125–137, June 2005. 2
- [31] Y. Tian. An analytical formula of population gradient for two-layered relu network and its applications in convergence and critical point analysis. In *Proceedings of the fifth International Conference on Learning Representations (ICLR)*, 2017. 1
- [32] M. Weiler, F. A. Hamprecht, and M. Storath. Learning steerable filters for rotation equivariant cnns. In *2018 IEEE Conference on Computer Vision and Pattern Recognition (CVPR)*, 2018. 2
- [33] D. Worrall, S. Garbin, D. Turmukhambetov, and G. Brostow. Harmonic networks: Deep translation and rotation equivariance. In *2017 IEEE Conference on Computer Vision and Pattern Recognition (CVPR)*, pages 7168–7177, 2017. 2
- [34] H. Yao, L. Chuyi, H. Dan, and Y. Weiyu. Gabor feature based convolutional neural network for object recognition in natural scene. In *Proceedings of the third International Conference on Information Science and Control Engineering (ICISCE)*, pages 386–390, July 2016. 2
- [35] A. Younesi and M. C. Amirani. Gabor filter and texture based features for palmprint recognition. *Procedia Computer Science*, 108:2488 – 2495, 2017. International Conference on Computational Science, ICCS 2017, 12-14 June 2017, Zurich, Switzerland. 2
- [36] H. Zhang, B. Chen, D. Guo, and M. Zhou. WHAI: Weibull hybrid autoencoding inference for deep topic modeling. In *Proceedings of the sixth International Conference on Learning Representations (ICLR)*, 2018. 1
- [37] H. Zhang, B. Chen, Z. Wang, and H. Liu. Deep max-margin discriminant projection. *IEEE Transactions on Cybernetics*, pages 1–13, 2018. 1